International Journal of General Systems
Vol. 42, No. 5, July 2013, 519–541

Stationary Dissipative Solitons of Model G

Matthew Pulver[a†] and Paul A. LaViolette[b‡]

[a]*Blue Science, Los Angeles, California USA*
[b]*Starburst Foundation, Schenectady, New York USA*
(*Received 7 July 2012; final version received 12 February 2013*)

Model G, the earliest reaction-diffusion system proposed to support the existence of solitons, is shown to do so under distant steady-state boundary conditions. Subatomic particle physics phenomenology, including multi-particle bonding, movement in concentration gradients, and a particle structure matching Kelly's charge distribution model of the nucleon, are observed. Lastly, it is shown how a three-variable reversible Brusselator, a close relative of Model G, can also support solitons.

Keywords: Brusselator; dissipative soliton; Model G; reaction-diffusion system; subquantum kinetics; Turing instability; Turing wave

1. Introduction

Since the seminal work of Turing (1952), stationary and oscillating patterns have been studied and observed in a variety of open reaction-diffusion (R-D) systems, one example being the three-variable Belousov-Zhabotinsky reaction (Winfree, 1974; Zaikin and Zhabotinsky, 1970). The Brusselator, first proposed in 1968, is the simplest R-D system known to produce wave patterns of precise wavelength. It is a two-variable R-D system specified by the following reactions (Lefever, 1968; Nicolis and Prigogine, 1977):

$$\mathrm{A} \rightarrow \mathrm{X} \tag{1a}$$

$$\mathrm{B} + \mathrm{X} \rightarrow \mathrm{Y} + \mathrm{D} \tag{1b}$$

$$2\mathrm{X} + \mathrm{Y} \rightarrow 3\mathrm{X} \tag{1c}$$

$$\mathrm{X} \rightarrow \mathrm{E}. \tag{1d}$$

In the Brusselator, only the X and Y reactants are variable while A, B, D, and E are held constant. The value of either source reactant A or B serves as the bifurcation parameter determining whether the system is able to spawn a dissipative structure. But because their concentrations are kept invariant, the system's criticality remains uniform throughout the reaction volume and, in the case where the system is supercritical, gives rise to a nonlocalized dissipative structure. Herschkowitz-Kaufman

†matt@blue-science.org

‡plaviolette@starburstfound.org

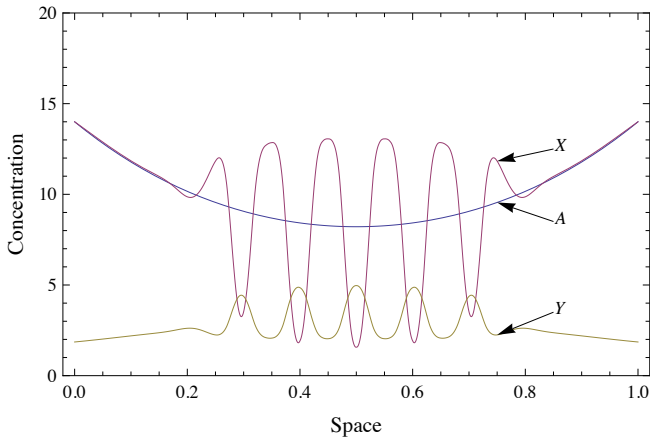

(a) Box length = 1.

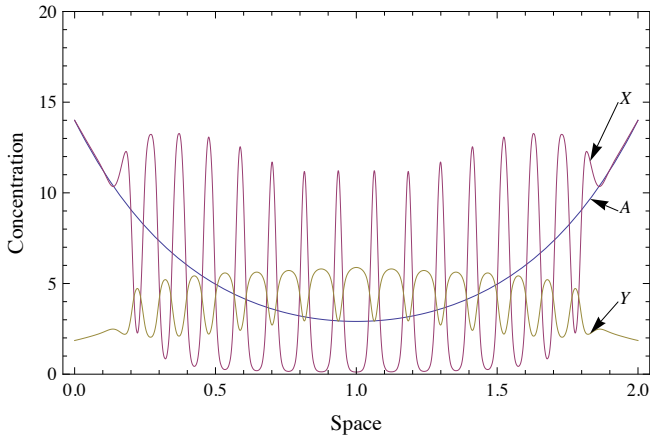

(b) Box length = 2.

Figure 1. (a) The localized steady state dissipative structure of Herschkowitz-Kaufman and Nicolis (1972) in a 1D box of length 1. (b) Same system parameters with box length = 2, demonstrating the dependence of structure localization upon system boundaries.

and Nicolis (1972), on the other hand, have been able to create a localized dissipative structure by allowing A to vary while holding its concentration fixed at the system boundaries at a level above the critical threshold value A_c. Consumption of A through reaction (1a) creates the formation of an "A-well" which in the steady state forms a hypercosine function solution satisfying the relation $A = D_A \nabla^2 A$. The reactions become supercritical wherever A attains a value less than A_c, allowing X and Y to self-organize a dissipative structure localized in the A-well's interior.

While Herschkowitz-Kaufman and Nicolis (1972) note that this version of the Brusselator produces a dissipative structure that is localized within boundaries that are distinct from the reaction system boundaries, a dissipative structure generated in this fashion is not an autonomous entity since its morphology depends on the particular placement and extent of those boundaries; see Figure 1. If these boundaries are sufficiently expanded or removed, the localized X-Y structure dissolves. In the Brusselator, the depth of the A-well determines whether X and Y will form an ordered pattern, but not vice versa. That is, the X and Y values forming the soliton do not themselves affect the concentration of A; they do not determine the character of the A-well which in turn determines whether or not the X-Y ordered state can exist.

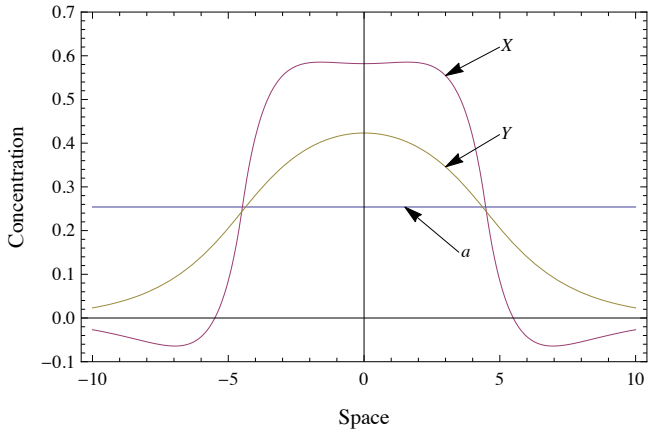

Figure 2. Localized dissipative structure of Koga and Kuramoto (1980). $D_{\mathrm{X}} = 1$, $D_{\mathrm{Y}} = 5$, $a = 0.254$, $b = 0.5$, $c = 0.5$.

Koga and Kuramoto (1980) simulated a localized dissipative structure supported by a system defined by the equations:

$$\frac{\partial \mathrm{X}}{\partial \mathrm{t}} = D_{\mathrm{X}} \nabla^2 \mathrm{X} - \mathrm{X} - \mathrm{Y} - H(\mathrm{X} - a) \tag{2a}$$

$$\frac{\partial \mathrm{Y}}{\partial \mathrm{t}} = D_{\mathrm{Y}} \nabla^2 \mathrm{Y} + b\mathrm{X} - c\mathrm{Y} \tag{2b}$$

where a, b, c are system constants, and H is the Heaviside step function. In the center of the soliton, there is a finite region in which $\mathrm{X} > a$ and thus $H = 1$, outside of which $H = 0$. See Figure 2. With this mechanism the structure maintains its localized form. It is important to note, however, that an equation that uses the unit step H in this way is not expressible as a finite set of reaction equations (e.g. eqs. (1)) and therefore we would not classify this dissipative system as a R-D system.

However, a minor variation of the Brusselator, a three-variable R-D system known as Model G, has been theorized in 1980 to support localized, self-stabilizing Turing patterns within a subcritical environment when the values of its system parameters are properly chosen (LaViolette, 1985, 1994, 2008, 2010). It is able to form a true dissipative soliton, one whose structure is stable, autonomous, localized, and unaffected by the positions of the system boundaries. Its system of partial differential equations are derived from a simple set of kinetic reaction equations with diffusion, and is in fact the earliest R-D system proposed to support solitons. Others have since reported simulation results of dissipative solitons, such as Schenk *et al.* (1998) who investigated a two-variable system of the FitzHugh-Nagumo (FN) type. Surveys of dissipative solitons produced by dissipative systems of both the R-D and non-R-D types are given by Purwins *et al.* (2005), Bödeker (2007) and Vanag and Epstein (2007).

Dissipative solitons have generated substantial interest because of the variety of particle-like properties they have been shown to produce such as scattering, reflection, particle-particle bonding, orbital motion, particle annihilation, and particle replication (Bode *et al.*, 2002; Bödeker, 2007; Liehr *et al.*, 2004; Nishiura *et al.*, 2005; Purwins *et al.*, 2005; Schenk *et al.*, 1998; Vanag and Epstein, 2007). Previous publications have demonstrated that Model G can form the basis for a unified field theory that effectively accounts for a variety of microphysical and macrophysical phenomena (LaViolette, 1985, 1986, 1992, 2005, 2008, 2010). In this paper, we

present computer simulation results carried out for the first time on this promising reaction system.

2. Model G

Model G is a modification of the Brusselator in which a third intermediary variable G is inserted into the first reaction step (1a). It is specified by the following five transformations:

$$\mathrm{A} \underset{k_{-1}}{\overset{k_1}{\rightleftharpoons}} \mathrm{G} \tag{3a}$$

$$\mathrm{G} \underset{k_{-2}}{\overset{k_2}{\rightleftharpoons}} \mathrm{X} \tag{3b}$$

$$\mathrm{B} + \mathrm{X} \underset{k_{-3}}{\overset{k_3}{\rightleftharpoons}} \mathrm{Y} + \mathrm{Z} \tag{3c}$$

$$2\mathrm{X} + \mathrm{Y} \underset{k_{-4}}{\overset{k_4}{\rightleftharpoons}} 3\mathrm{X} \tag{3d}$$

$$\mathrm{X} \underset{k_{-5}}{\overset{k_5}{\rightleftharpoons}} \Omega \tag{3e}$$

where reaction step (1a) is replaced by the two reactions (3a, 3b). This R-D system is represented by the following system of partial differential equations:

$$\frac{\partial \mathrm{G}}{\partial \mathrm{t}} = D_{\mathrm{G}} \nabla^2 \mathrm{G} - (k_{-1} + k_2)\mathrm{G} + k_{-2}\mathrm{X} + k_1 \mathrm{A} \tag{4a}$$

$$\begin{aligned} \frac{\partial \mathrm{X}}{\partial \mathrm{t}} = {} & D_{\mathrm{X}} \nabla^2 \mathrm{X} + k_2 \mathrm{G} - (k_{-2} + k_3 \mathrm{B} + k_5)\mathrm{X} \\ & + k_{-3}\mathrm{ZY} - k_{-4}\mathrm{X}^3 + k_4 \mathrm{X}^2 \mathrm{Y} + k_{-5}\Omega \end{aligned} \tag{4b}$$

$$\frac{\partial \mathrm{Y}}{\partial \mathrm{t}} = D_{\mathrm{Y}} \nabla^2 \mathrm{Y} + k_3 \mathrm{BX} - k_{-3}\mathrm{ZY} + k_{-4}\mathrm{X}^3 - k_4 \mathrm{X}^2 \mathrm{Y}. \tag{4c}$$

Since the forward kinetic constants have values much greater than the reverse kinetic constants, the reactions have the overall tendency to proceed irreversibly to the right. Nevertheless, the reverse reaction G ← X in eq. (3b) plays an important role. This allows the concentration of the X variable to influence the concentration value of the G variable which in turn serves as the system's bifurcation parameter. So, because Model G's bifurcation parameter is able to vary in both time and space, and be influenced by its X variable which participates in forming a soliton-like dissipative structure, this reaction system is able to nucleate a structure which, in the positive Y polarity (negative X), is autonomous and self-stabilizing. All that is needed is a momentary localized fluctuation in one of the reactants sufficiently large in amplitude and spatiotemporal breadth to initiate the growth of the soliton. This technique of allowing a third reactant to serve as a variable bifurcation parameter for the other two reactants is a recipe general enough for potential applicability to other dissipative-structure-producing R-D systems, allowing them to support dissipative solitons as well.

The seed fluctuation may be in the form of an extra term that is added to the R-D equations, or it may be directly incorporated within the R-D equations by

representing the concentration of each reactant with a stochastic term. Such "zero-point" fluctuations would be present if each reactant is comprised of a plurality of constituent units (e.g., X-ons, Y-ons, G-ons) which engage in Markovian birth-death transformations.

A positive polarity seed fluctuation (negative X, or positive Y), arising spontaneously in this fashion, is able to spawn a periodic structure even when the system is initially in a *subcritical* homogeneous steady state. The Brusselator, on the other hand, must always begin from an initially supercritical homogeneous steady state. As a result, its structures are always destined to fill the entire reaction volume to its supercritical limits. This autogenic ability, wherein a stable dissipative soliton can form spontaneously out of system noise, is an important distinctive feature of Model G. LaViolette (1985, 2010) has shown that this feature makes Model G a promising candidate for modeling the formation of subatomic particles out of the zero-point energy continuum vacuum state. How Model G has been employed to model subatomic particles is further elaborated on in Section 3.1.

2.1 *Nondimensionalization*

In analyzing eqs. (4), we first pass to dimensionless variables. This reduces the number of independent system parameters by seven, significantly simplifying the goal of finding a particular set of system parameters (eqs. (17) below) that support the formation of a stable soliton. In addition, this conveniently scales the dimensionless space, time, and concentration potential values to the order of unity in the vicinity of the soliton formation event.

We assume that the three diffusion constants D_{G}, D_{X}, D_{Y}, four concentrations A, B, Z, Ω, and the ten kinetic reaction rates $k_{\pm i}$ are constant in time and space.

The dimensional space, time, and concentration variables x, y, z, t, G, X, Y are converted to their corresponding dimensionless variables x, y, z, t, G, X, Y via the following substitutions:

$$\begin{aligned} \mathrm{x} = \mathrm{L}x, \quad \mathrm{y} = \mathrm{L}y, \quad \mathrm{z} = \mathrm{L}z, \quad \mathrm{t} = \mathrm{T}t \\ \mathrm{G}(\mathrm{x},\mathrm{y},\mathrm{z},\mathrm{t}) = \mathrm{C}G(x,y,z,t) \\ \mathrm{X}(\mathrm{x},\mathrm{y},\mathrm{z},\mathrm{t}) = \mathrm{C}X(x,y,z,t) \\ \mathrm{Y}(\mathrm{x},\mathrm{y},\mathrm{z},\mathrm{t}) = \mathrm{C}Y(x,y,z,t) \end{aligned} \tag{5}$$

where the time, space, and concentration constants are defined, respectively, as:

$$\mathrm{T} \equiv \frac{1}{k_{-2}+k_5}, \quad \mathrm{L} \equiv \sqrt{D_{\mathrm{G}}\mathrm{T}}, \quad \mathrm{C} \equiv \frac{1}{\sqrt{k_4\mathrm{T}}}. \tag{6}$$

These substitutions allow for eqs. (4) to be expressed in terms of dimensionless variables:

$$\frac{\partial G}{\partial t} = \nabla^2 G - qG + gX + a \tag{7a}$$

$$\frac{\partial X}{\partial t} = d_{\mathrm{x}}\nabla^2 X + pG - (1+b)X + uY - sX^3 + X^2Y + w \tag{7b}$$

$$\frac{\partial Y}{\partial t} = d_{\mathrm{y}}\nabla^2 Y + bX - uY + sX^3 - X^2Y \tag{7c}$$

where

$$d_{\mathrm{x}} \equiv \frac{D_{\mathrm{X}}}{D_{\mathrm{G}}}, \quad d_{\mathrm{y}} \equiv \frac{D_{\mathrm{Y}}}{D_{\mathrm{G}}},$$
$$a \equiv \frac{k_1\sqrt{k_4}}{(k_{-2}+k_5)^{3/2}}\mathrm{A}, \quad b \equiv \frac{k_3}{k_{-2}+k_5}\mathrm{B}, \quad g \equiv \frac{k_{-2}}{k_{-2}+k_5}, \quad p \equiv \frac{k_2}{k_{-2}+k_5}, \tag{8}$$
$$q \equiv \frac{k_{-1}+k_2}{k_{-2}+k_5}, \quad s \equiv \frac{k_{-4}}{k_4}, \quad u \equiv \frac{k_{-3}}{k_{-2}+k_5}\mathrm{Z}, \quad w \equiv \frac{\sqrt{k_4}k_{-5}}{(k_{-2}+k_5)^{3/2}}\Omega.$$

The vector operator ∇ is taken with respect to the dimensional x, y, z terms in eqs. (4) and with respect to the dimensionless x, y, z in eqs. (7). Since there will never be ambiguity in its context, we use the same symbol ∇ for both.

2.2 *Redimensionalization*

The dimensional diffusion coefficients, kinetic constants, and constant concentrations A, B, Z, Ω are given as follows when expressed in terms of their dimensionless counterparts and T, L, C:

$$D_{\mathrm{G}} = \frac{\mathrm{L}^2}{\mathrm{T}}, \quad D_{\mathrm{X}} = \frac{\mathrm{L}^2}{\mathrm{T}}d_{\mathrm{x}}, \quad D_{\mathrm{Y}} = \frac{\mathrm{L}^2}{\mathrm{T}}d_{\mathrm{y}},$$
$$k_1\mathrm{A} = \frac{\mathrm{C}}{\mathrm{T}}a, \quad k_2 = \frac{1}{\mathrm{T}}p, \quad k_3\mathrm{B} = \frac{1}{\mathrm{T}}b, \quad k_4 = \frac{1}{\mathrm{C}^2\mathrm{T}}, \quad k_5 = \frac{1}{\mathrm{T}}(1-g), \tag{9}$$
$$k_{-1} = \frac{1}{\mathrm{T}}(q-p), \quad k_{-2} = \frac{1}{\mathrm{T}}g, \quad k_{-3}\mathrm{Z} = \frac{1}{\mathrm{T}}u, \quad k_{-4} = \frac{1}{\mathrm{C}^2\mathrm{T}}s, \quad k_{-5}\Omega = \frac{\mathrm{C}}{\mathrm{T}}w.$$

2.3 *Homogeneous Steady State*

The homogeneous steady state is one in which

$$0 = \frac{\partial G}{\partial t} = \frac{\partial X}{\partial t} = \frac{\partial Y}{\partial t} \tag{10a}$$
$$\mathbf{0} = \nabla G = \nabla X = \nabla Y. \tag{10b}$$

Under these conditions the differential equations (7) become algebraic with G, X, Y having the following respective solutions:

$$G_0 = \frac{a+gw}{q-gp}, \quad X_0 = \frac{pa+qw}{q-gp}, \quad Y_0 = \frac{sX_0^2+b}{X_0^2+u}X_0. \tag{11}$$

2.4 *Concentration Potentials*

It proves useful to consider concentration values relative to the homogeneous steady state (LaViolette, 1985, 1994, 2008). These *concentration potentials* are defined as:

$$\varphi_G \equiv G - G_0, \quad \varphi_X \equiv X - X_0, \quad \varphi_Y \equiv Y - Y_0. \tag{12}$$

Eqs. (7) are expressed in terms of concentration potentials as:

$$\frac{\partial \varphi_G}{\partial t} = \nabla^2 \varphi_G - q\varphi_G + g\varphi_X \tag{13a}$$

$$\begin{aligned}\frac{\partial \varphi_X}{\partial t} &= d_{\mathrm{x}} \nabla^2 \varphi_X + p\varphi_G - (1+b)\varphi_X + u\varphi_Y \\ &\quad - s\left((\varphi_X + X_0)^3 - X_0^3\right) + \left((\varphi_X + X_0)^2(\varphi_Y + Y_0) - X_0^2 Y_0\right)\end{aligned} \tag{13b}$$

$$\begin{aligned}\frac{\partial \varphi_Y}{\partial t} &= d_{\mathrm{y}} \nabla^2 \varphi_Y + b\varphi_X - u\varphi_Y \\ &\quad + s\left((\varphi_X + X_0)^3 - X_0^3\right) - \left((\varphi_X + X_0)^2(\varphi_Y + Y_0) - X_0^2 Y_0\right).\end{aligned} \tag{13c}$$

This substitution is especially important when calculating numerical solutions for G, X, and Y that correspond to a dissipative soliton, which, as will be seen below, consists of small deviations about the homogeneous steady state values G_0, X_0, and Y_0.

3. Particle Formation and Structure in Model G

We examine the evolution of the system in 1, 2, and 3 dimensions of space. In the case of 2 and 3 dimensions, circular and spherical symmetry, respectively, are imposed upon the system.[1]

Each concentration potential is a function of both position x in 1D (radius r in the case of 2D and 3D) and time t. The reaction spatial domain and total time is specified as $-50 \le x \le 50$ in 1D ($0 \le r \le 50$ in 2D and 3D) and $0 \le t \le 100$.

The boundary conditions for 1D are:[2]

$$\forall x \in [-50, 50] : \forall t \in [0, 100] :$$

$$\varphi_G(x,t) \ge -G_0, \quad \varphi_X(x,t) \ge -X_0, \quad \varphi_Y(x,t) \ge -Y_0 \tag{14a}$$

$$\varphi_G(x,0) = 0, \quad \varphi_X(x,0) = 0, \quad \varphi_Y(x,0) = 0 \tag{14b}$$

$$\varphi_G(\pm 50, t) = 0, \quad \varphi_X(\pm 50, t) = 0, \quad \varphi_Y(\pm 50, t) = 0. \tag{14c}$$

For 2D and 3D, the boundary conditions are:

$$\forall r \in [0, 50] : \forall t \in [0, 100] :$$

$$\varphi_G(r,t) \ge -G_0, \quad \varphi_X(r,t) \ge -X_0, \quad \varphi_Y(r,t) \ge -Y_0 \tag{15a}$$

$$\varphi_G(r,0) = 0, \quad \varphi_X(r,0) = 0, \quad \varphi_Y(r,0) = 0 \tag{15b}$$

$$\varphi_G(50,t) = 0, \quad \varphi_X(50,t) = 0, \quad \varphi_Y(50,t) = 0 \tag{15c}$$

$$(\varphi_G)_r(\varepsilon,t) = 0, \quad (\varphi_X)_r(\varepsilon,t) = 0, \quad (\varphi_Y)_r(\varepsilon,t) = 0. \tag{15d}$$

The subscript r in eqs. (15d) denote the partial derivative with respect to r.

[1] The circular and spherical symmetry conditions in 2 and 3 dimensions that are imposed upon the system are due entirely to the limited availability of computational resources for this research project at the time of this publication. The mathematics, as well as the simulation software, is general enough for these symmetry restrictions to be removed—it is only a matter of acquiring sufficient computational time (CPU cycles) and space (memory) to carry out the simulations.

[2] "$\forall$" is the universal quantifier symbol. The first line of eqs. (14) reads "For all x between -50 and 50, and for all t from 0 to 100:"

Since the soliton shall be centered at the point $r = 0$, the boundary condition at $r = 0$ must not constrain the concentration potential values at this point. Instead, the boundary condition is placed upon their first order derivatives with respect to r. Under the imposed constraints of angular symmetry in 2D and 3D, these derivatives must vanish.

Epsilon, ε, is a small positive number to numerically approximate zero. $\varepsilon \neq 0$ for computational reasons only, due to the indeterminate form the rotationally-symmetric Laplacian takes in 2D and 3D at $r = 0$:

$$\nabla^2\varphi = \frac{\partial^2\varphi}{\partial r^2} + \frac{n-1}{r}\frac{\partial\varphi}{\partial r} \tag{16}$$

where $n \in \{1, 2, 3\}$ is the number of spatial dimensions. The point at $r = 0$ is smoothly approximated since the limit of $\nabla^2\varphi$ as $r \to 0$ is always finite. The numerical simulations in this work use $\varepsilon = 10^{-9}$.

There are an infinite continuum of parameter values that allow for the creation of a stationary soliton. The particular set of values that is investigated in this article are the following:

$$\begin{aligned} d_{\mathrm{x}} = 1, \quad d_{\mathrm{y}} = 12, \quad a = 14, \quad b = 29, \quad g = 1/10, \\ p = 1, \quad q = 1, \quad s = 0, \quad u = 0, \quad w = 0. \end{aligned} \tag{17}$$

If the system is left to evolve according to eqs. (13–17), the concentrations will remain at their homogeneous steady state values, i.e. $0 = \varphi_{G} = \varphi_{X} = \varphi_{Y}$ for all r and t. In order to initiate the formation of a soliton, we introduce a momentary seed fluctuation in the X variable specified as χ:

$$\chi(r,t) \equiv -e^{-\frac{r^2}{2}} e^{-\frac{(t-10)^2}{18}}. \tag{18}$$

The time evolution of this fluctuation is graphed in Figure 3 as $\chi/10$ for four particular points in time.

For one spatial dimension, r in the above equation is replaced with x. This seed fluctuation is incorporated into the system by adding χ to the right-hand side of eq. (13b). In addition, substituting values (17) into eqs. (13), yields the following system of nonlinear PDEs:

$$\frac{\partial\varphi_{G}}{\partial t} = \nabla^2\varphi_{G} - \varphi_{G} + \varphi_{X}/10 \tag{19a}$$

$$\frac{\partial\varphi_{X}}{\partial t} = \nabla^2\varphi_{X} + \varphi_{G} - 30\varphi_{X} - 4060/9 + (\varphi_{X} + 140/9)^2(\varphi_{Y} + 261/140) + \chi \tag{19b}$$

$$\frac{\partial\varphi_{Y}}{\partial t} = 12\nabla^2\varphi_{Y} + 29\varphi_{X} + 4060/9 - (\varphi_{X} + 140/9)^2(\varphi_{Y} + 261/140). \tag{19c}$$

Eqs. (19), along with the boundary conditions (14 or 15), may then be numerically solved on a computer.

3.1 *Particle Structure in 3D*

Figure 4 shows the computer-simulated evolution of φ_{G}, φ_{X}, and φ_{Y} under eqs. (19) in three spatial dimensions, subject to boundary conditions (15) and graphed at times $t = 0$, $t = 10$, $t = 13$ and $t = 20$.

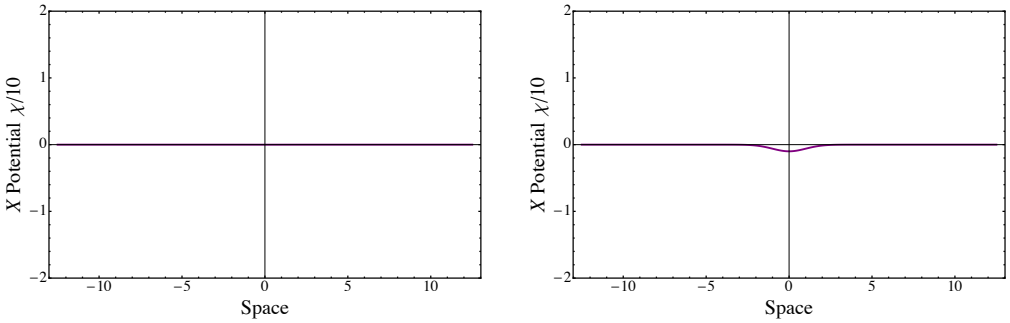

(a) $t = 0$ (b) $t = 10$

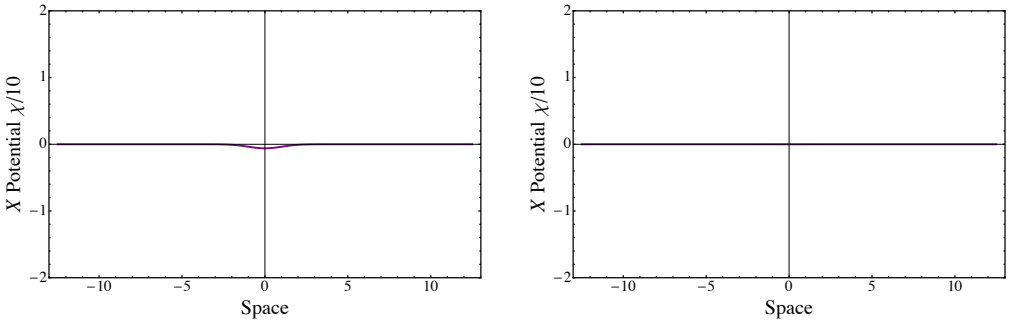

(c) $t = 13$ (d) $t = 20$

Figure 3. The seed fluctuation $\chi/10$.

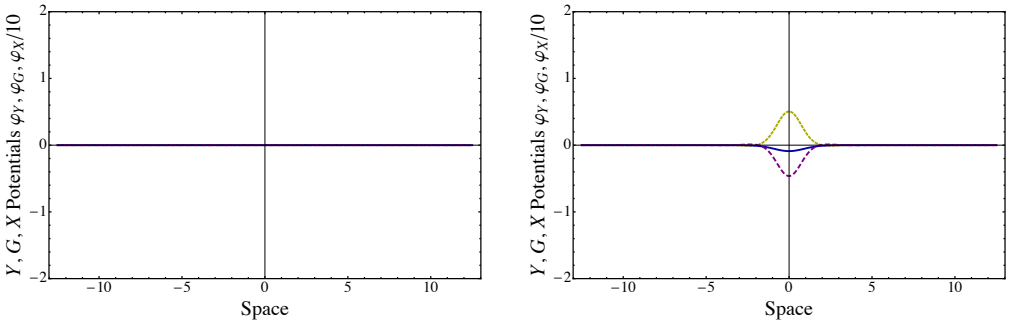

(a) $t = 0$ (b) $t = 10$

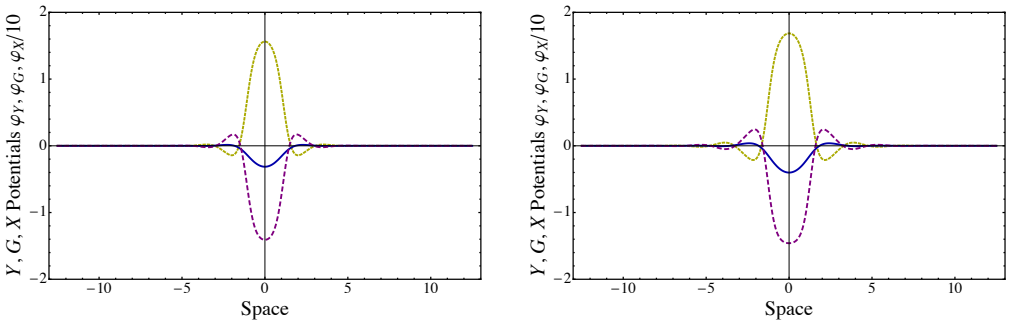

(c) $t = 13$ (d) $t = 20$

Figure 4. 3D Particle Formation. In frames with $t > 0$, the three curves from top to bottom along the central vertical axis, respectively, are φ_Y (yellow), φ_G (blue), and $\varphi_X/10$ (magenta). The stable soliton pattern that emerges is induced by the seed fluctuation of Figure 3.

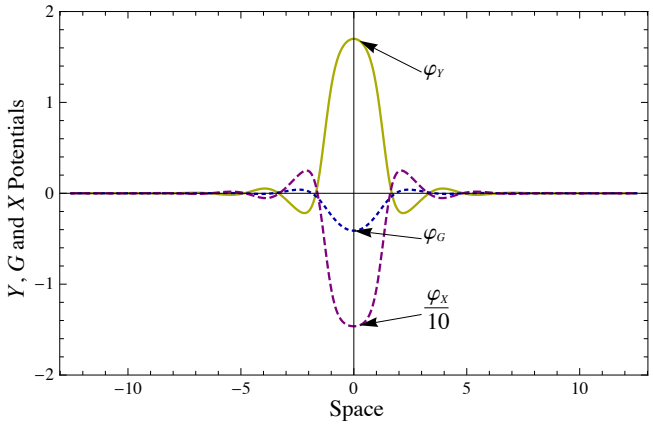

(a) Spherically-symmetric 3D stationary particle.

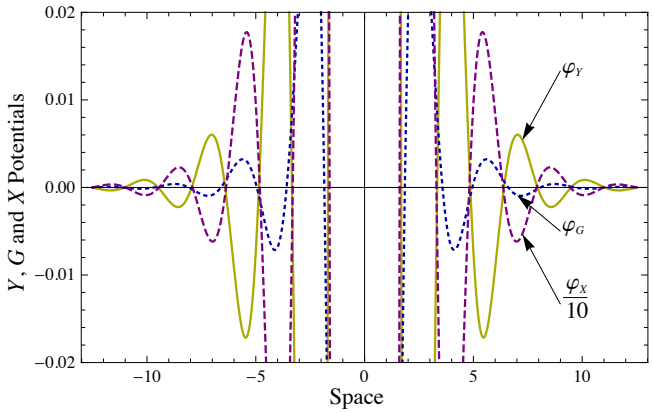

(b) Zoomed 100×.

Figure 5. (a) Spherically-symmetric 3D stationary particle formed from eqs. (19) and boundary conditions (15). (b) Same data zoomed 100× vertically.

The system converges to the stationary structure shown in Figure 5(a). This stable soliton is what is identified in Model G as an individual particle. These simulation results show that the reaction variables produce a periodic pattern of precise wavelength, $\lambda_0 = 3.08$ units, that progressively decreases in amplitude as it extends outward from a central bell-shaped core. Figure 5(b) exhibits the extent of the periodicity of the particle's potential fields by zooming the vertical axis of the simulation 100×.

The subquantum kinetics physics methodology developed by LaViolette (1985, 2008, 2010, 2012) postulates that subatomic particles are electric and gravity potential solitons. It identifies the φ_G variable with gravity potential and the φ_X and φ_Y variables with electric potential. Negative φ_G values are associated with positive, matter-attracting gravitational mass and positive φ_G values are associated with negative, matter-repelling gravitational mass. Positive and negative φ_Y values (negative and positive φ_X values) are associated respectively with positive and negative charge, the φ_X and φ_Y variables having a reciprocal relation to one another. Since the φ_G and φ_X potentials are closely coupled in Model G due to the linkage of species G and X through both forward and reverse reactions, subquantum kinetics predicts that the electric and gravitational potentials should be closely coupled: negative gravity potential with positive electric potential. Thus in subquantum kinetics, subatomic particles are envisioned as local field potential inhomogeneities.

Since these particular inhomogeneities share a common Turing wave pattern morphology, this leads to a natural quantization of these fields into identical particles. This is reminiscent of the quantization of fermionic matter fields in quantum field theory which is invoked to explain why those fields' particles are identical.

The simulation displayed in Figures 4 and 5 would be interpreted in subquantum kinetics as the nucleation of a neutral subatomic particle, a neutron for example, being nucleated by a positive charge polarity electric potential fluctuation emerging from the subquantum zero-point energy field. In this case the particle's core has a positive electric potential coinciding with a negative gravity potential and creating a local stabilizing supercritical domain. In subquantum kinetics, such fluctuations can trigger particle nucleation even though they themselves have a field energy potential magnitude much smaller than that of the particle they nucleate. A negatively charged fluctuation would lead to the formation of an antimatter particle having a core with a negative electric potential coinciding with a positive gravity potential. But, as LaViolette (1985) has pointed out, such negative charge polarity fluctuations emerging from system noise where the reaction system is initially subcritical, as would be the case for the primordial vacuum state, fail to nucleate a particle. He notes that Model G's ability to nucleate solitons with an inherent polarity bias favoring the matter state is a feature that is advantageous in the application to cosmology where nature has favored the primordial creation of matter over antimatter.

These modeling results confirm LaViolette's 1985 prediction that Model G should generate a dissipative space structure whose field potential has this same form: a gaussian core surrounded by an extended asymptotic field periodicity. He proposed that such a field potential could serve as a useful model of a subatomic particle provided that the reaction system parameters are chosen such that the wavelength of the soliton's oscillatory tail equals the subatomic particle's Compton wavelength. He demonstrated that this periodic tail, which he termed the particle's *Turing wave*, accounts for the experimental results of both particle diffraction and orbital quantization (LaViolette, 1985, 1994, 2010).

Later, LaViolette (2008, 2010) noted that the φ_Y (and φ_X) wave pattern predicted for Model G's Turing wave soliton field pattern has a morphology very similar to the charge distribution model that Kelly (2002) derived for the core of the nucleon by analyzing form factor data obtained from high energy electron beam particle scattering experiments. Kelly obtained a best fit to this scattering data by assuming that the nucleon's charge and magnetization distribution had the form of a gaussian core surrounded by a periodicity having a wavelength approximating the nucleon's Compton wavelength. The simulation results presented here further support this suggestion in that they indicate that the φ_X and φ_Y field pattern generated by Model G displays morphological features similar to those of the radial electric charge distribution in the neutron and proton and should therefore serve as an appropriate soliton field structure for modeling subatomic particles.

The amplitude of the φ_X (or φ_Y) field maxima forming the simulated Model G soliton are observed to decline as $r^{-3.7}$ at $r \approx 2\lambda_0$, as r^{-7} at $r \approx 4\lambda_0$, and as r^{-10} at $r \approx 6\lambda_0$. This may be compared with r^{-7} in standard theories for the radial decline of the nuclear force. Because of this rapid decline, the product of the Turing pattern field amplitude with incremental shell volume diminishes toward zero for shells of successively greater radius, and the sum of these shell product increments converges to a finite value. A finite value for the soliton negentropy makes Model G attractive as a model of a subatomic particle since subquantum kinetics identifies the φ_X, φ_Y field magnitudes forming the Model G soliton, with both the electric field forming the particle's core and with the particle's inertial mass (LaViolette,

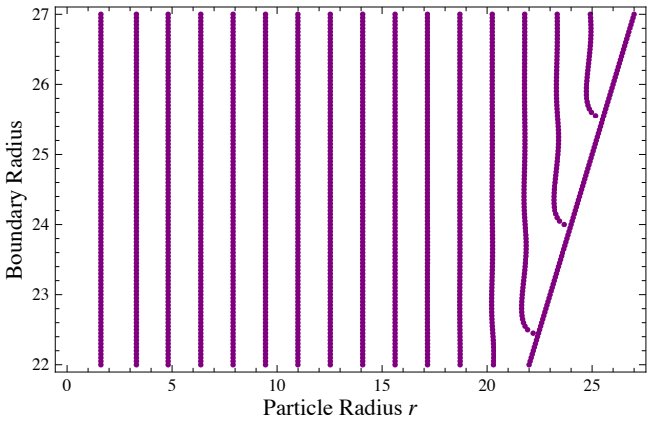

(a) Zeroes of φ_X with a variable system boundary.

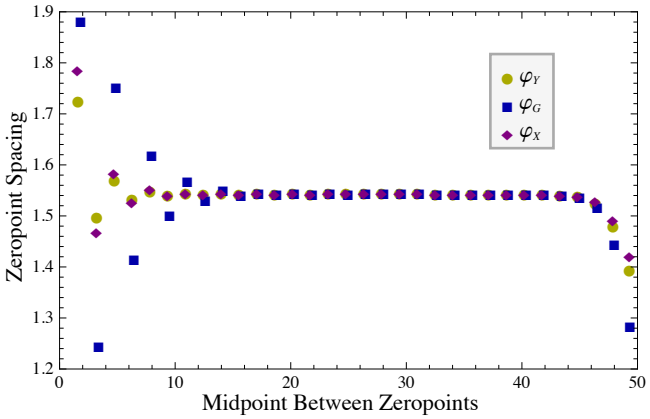

(b) Differences and locations of zeroes for φ_Y, φ_G, and φ_X.

Figure 6. The Turing wavelength is independent of the distance between the particle core and system boundary, and is the same value for each reactant. Figure (a) shows the periodic locations of the zeroes of φ_X (horizontal axis) for a spherically-symmetric 3D particle centered at $r = 0$, with a variable system radius (vertical axis), demonstrating that the Turing wavelength is independent of the size of the enclosing system volume. Figure (b) shows the successive differences between zeroes for φ_Y, φ_G, and φ_X (vertical axis) for a 1D particle at the midpoints between each zero-pair (horizontal axis). The central alignment of zero differences demonstrates that the Turing wavelength is the same for each reactant, equal to 3.08 (twice the distance between zeroes). Similar results were found for circularly and spherically symmetric 2D and 3D particles, respectively.

1985, 2010).

We also report the simulation results of producing ordered patterns with Model G where the reaction vessel size was progressively increased. The Turing pattern periodicity was found to persist to the vessel boundaries and to maintain a constant wavelength as the vessel size was expanded. This is shown in Figure 6(a) which plots the radial distance locations of the φ_X zero values (horizontal axis) against the radial size of the spherical reaction volume (vertical axis), and shows how the particle's fields adjust in the vicinity of the steady-state boundary conditions. The persistence of this wave pattern and invariance of its wavelength with increasing vessel size demonstrates that the Turing pattern is independent of the boundary conditions. These results also confirm the predictions of LaViolette (1994, 2008) that the Model G Turing pattern should persist outward to large radial distances in order to properly model the particle diffraction phenomenon. The pattern, though, would have the inherent radial limit at the radial distance where the noise amplitude present in the stochastic variation of each reactant concentration exceeds the Turing wave pattern amplitude.

3.2 *Comparison of Particle Structures Simulated in 1D, 2D, and 3D*

When Model G is simulated in 1D and 2D, it produces particles whose cores are narrower and lower in amplitude, although their Turing wavelength remains the same. Figure 7 shows the 1D and 2D particles formed from eqs. (19) and boundary conditions (14) and (15), respectively. Compare these to Figure 5(a). Specific values of the structural characteristics of the 1D, 2D, and 3D particles are shown in Table 1. The *core radius*, Table 1, row (b), is defined as the inner-most zero-point field potential crossing r_0 (the least positive value for which $\varphi(r_0) = 0$) for each of the concentration potentials). Note that the radius in all cases is largest for φ_G and smallest for φ_X. The *core RMS radius*, the root mean square radius r_{RMS} listed in row (c), for each concentration potential in each of the three dimensions is calculated as:

$$\begin{aligned} r_{\mathrm{RMS}} &= \sqrt{\langle r^2 \rangle} \\ &= \sqrt{\frac{\int_S \varphi(r) r^2 dS}{\int_S \varphi(r) dS}}. \end{aligned} \tag{20}$$

The integral in the denominator of the above formula is the *core integral*, row (d), which is given by:

$$\int_S \varphi(r) dS = \begin{cases} \displaystyle\int_{-r_0}^{r_0} \varphi(r) dr & \text{in 1D,} \\ \displaystyle 2\pi \int_0^{r_0} \varphi(r) r dr & \text{in 2D,} \\ \displaystyle 4\pi \int_0^{r_0} \varphi(r) r^2 dr & \text{in 3D} \end{cases} \tag{21}$$

where the domain of integration S is the space within the *core radius* r_0 defined by each of the concentration potentials. The *full integral* values, row (e), use the same formulas as the core integral, but with r_0 going out to the system boundary.

The *Turing wavelength*, row (f), is found by first calculating successive differences between the zeroes of each of the 3 concentration potentials φ_Y, φ_G, φ_X. Figure 6(b) illustrates that this is a well-defined value for all 3 concentrations at a sufficient distance away from both the particle's central core and the system boundaries. The mean is calculated from the centrally-aligned data points and doubled (the distance between zeroes is a half-wavelength) resulting in a value of 3.08. This same λ_0 value to 3 significant figures was found in dimensions 1D, 2D, and 3D, where circular and spherical symmetry was imposed in the 2D and 3D cases, respectively.

4. Particle Physics in Model G

The solitons of Model G exhibit a number of properties resembling those commonly associated with subatomic particles. Earlier we noted that the morphology of the Model G solitons, their bell-shaped core surrounded by a Turing wave pattern of precise wavelength, has been found to be a good description of the core field of a nucleon. Another advantage mentioned earlier is that the full integral of the field potential converges to a finite value. Other characteristics discussed here include particle-particle bonding (i.e., equivalent to nuclear bonding), the gravitational

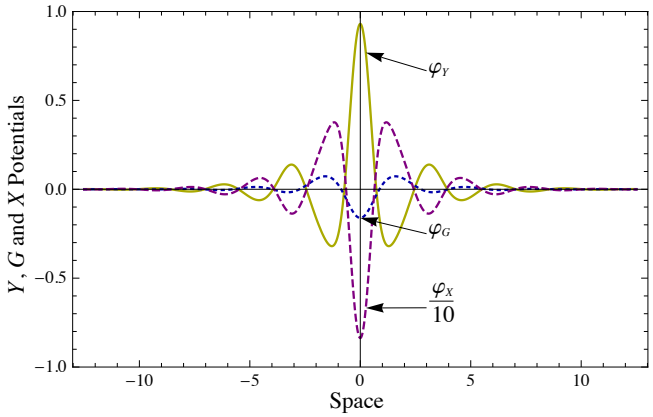

(a) 1D stationary particle.

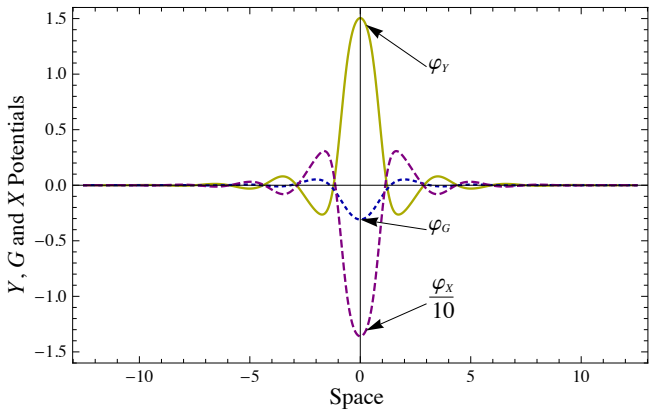

(b) Circularly-symmetric 2D stationary particle.

Figure 7. (a) 1D and (b) 2D stationary particles formed from eqs. (19) and boundary conditions (14, 15).

mass polarity in a particle with spin, and particle movement in a gravitational gradient.

4.1 *Multi-particle States in 1D*

The single particle discussed in Section 3 was seeded from a single gaussian fluctuation χ defined in eq. (18). In a similar way, multiple particles may be seeded from multiple gaussian fluctuations, and when seed fluctuations are spaced sufficiently close together, the resulting particles are able to coexist with one another at specific distances of separation. We examined cases in which particles are seeded in 1D from two and three gaussian seed fluctuations.

To seed two proximal particles, we define the double-gaussian seed fluctuation:

$$\chi_2(x,t) \equiv \chi(x + d_2/2, t) + \chi(x - d_2/2, t) \tag{22a}$$

$$d_2 = 3.303 \tag{22b}$$

and replace χ with χ_2 in eqs. (19) under boundary conditions (14). Figure 8(a) shows the stationary two-particle solution that the system converges to by $t = 100$. The final distance between the particles, defined as the distance between the core extrema of φ_X, is found to be 3.303, or about one Turing wavelength. This final particle distance is converged to even when d_2 in eq. (22a) is varied by small

Table 1. Particle structure values in dimensionless units.

			1D	2D	3D	2Dδ
(a)	Core amplitude	φ_Y	0.930	1.50	1.70	1.53
		φ_G	-0.161	-0.308	-0.411	-0.320
		φ_X	-8.36	-13.6	-14.6	-13.8
(b)	Core radius (first zero)	φ_Y	0.724	1.21	1.68	1.67
		φ_G	0.867	1.37	1.85	1.87
		φ_X	0.642	1.13	1.61	1.58
(c)	Core RMS radius	φ_Y	0.302	0.665	1.07	0.929
		φ_G	0.363	0.739	1.14	1.02
		φ_X	0.272	0.634	1.04	0.892
(d)	Core integral	φ_Y	0.806	3.12	13.2	6.31
		φ_G	-0.167	-0.710	-3.17	-1.44
		φ_X	-6.59	-26.3	-111	-53.6
(e)	Full integral	φ_Y	0.281	0.893	3.30	2.96
		φ_G	8.39×10^{-5}	2.88×10^{-3}	2.87×10^{-2}	-0.480
		φ_X	6.01×10^{-4}	0.128	1.93	-13.7
(f)	Turing wavelength		3.08	3.08	3.08	3.08

amounts both higher and lower. For example when $d_2 = 4$, the same 3.303 distance between the particles is converged to. For this reason we may conclude that the particles coexist in a *bonded* relationship to one another.

To seed three proximal particles, we define the triple-gaussian seed fluctuation:

$$\chi_3(x,t) \equiv \chi(x+d_3,t) + \chi(x,t) + \chi(x-d_3,t) \tag{23a}$$

$$d_3 = 3.314. \tag{23b}$$

Figure 8(b) shows the stationary three-particle solution the system converges to by $t = 100$. The final distance between the particles is 3.314, which again is a stable value that is converged to even when we make small variations in d_3. Future work will determine if such particle bonding also occurs in 2D and 3D simulations of Model G. Others working with the FN and FN-type models, who have simulated 2D dissipative solitons with oscillatory tails, also report particle-particle bonding and the formation of aggregate structures variously termed "clusters" or "molecules", although these are formed when the solitons have initial velocities relative to one another (Bode *et al.*, 2002; Purwins *et al.*, 2005; Schenk *et al.*, 1998). As is the case with the 1D simulations of Model G, these bound FN solitons are similarly found to align their concentration peaks with those of their partner.

When a two-particle simulation is performed with $d_2 = 6.628$, the two fluctuations being separated by the same distance as between the outer two particles of the three-particle stable state, two particles are initially created from the χ_2 seed fluctuations. However, the G potential well and Y potential hill formed in the space between them by the overlapping soliton tails provide a fertile environment that allows the spontaneous emergence of a third particle. This three-particle

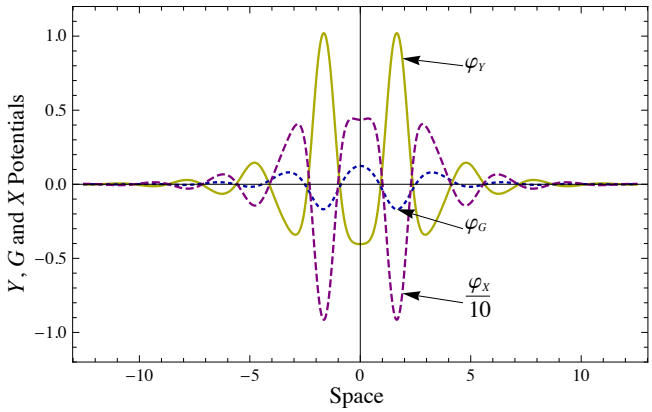

(a) Two 1D stationary bonded particles.

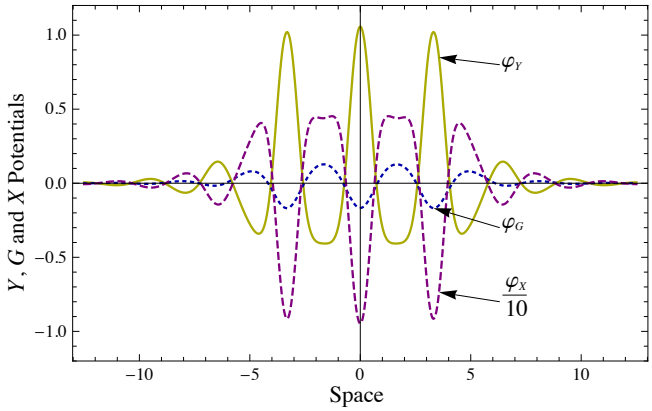

(b) Three 1D stationary bonded particles.

Figure 8. (a) Two and (b) three 1D stationary particles formed from eqs. (19) and boundary conditions (14), where χ is replaced by (a) χ_2 and (b) χ_3.

state then converges to the same three-particle state depicted in Figure 8(b). This confirms the earlier expectation that in Model G existing particles should produce favorable conditions facilitating additional particle autogenesis (LaViolette, 1985, 1994, 2010). Again, further work is needed to determine if mother-daughter particle creation also takes place in 2D and 3D simulations of Model G.

Two dimensional simulations of the FN model carried out by other researchers have also demonstrated the dissipative soliton particle replication phenomenon (Bödeker, 2007; Liehr *et al.*, 2003; Purwins *et al.*, 2005). In one case four particles move towards one another, collide, and form a stable bound cluster. Then a fifth soliton nucleates at the cluster's geometrical center where the concentration maxima of their innermost shells intersect and thereby produce a combined concentration maximum that is sufficiently great to induce spontaneous generation of the fifth particle. So this replication process occurs in the FN model in much the same fashion, although Model G spawns its progeny particles from initially stationary parent particles.

4.2 *Particle "Mass"*

Looking at Figure 5(a), it may appear as if the full integral of φ_G should be negative, due to the large central G-well, compared to the smaller G-hills that surround it. However, the contribution from these surrounding G-hill shells ultimately outweigh

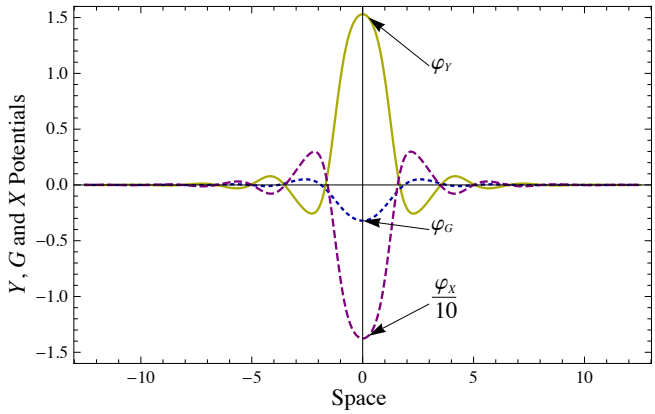

Figure 9. Circularly-symmetric 2D particle with gaussian diffusion coefficients, centered at the origin. It is conjectured that 3D particles may naturally form an etheric vortex through its core, producing a similar 2D cross-section perpendicular to the vortex.

the negative contribution of the G-well core and surrounding G-well shells yielding a positive value for the full integral of φ_G; see Table 1, row (e).

Subquantum kinetics interprets the full integral of φ_G as modeling a particle's gravitational mass which creates its long-range gravity field, positive mass being associated with a negative φ_G potential (LaViolette, 1985, 2010). So, to model a physically realistic particle of positive gravitational mass, the full integral of φ_G instead needs to be made negative. This could occur if the soliton core became broadened. To test this possibility, we have artificially broadened the core by introducing a variable diffusion coefficient. More specifically, we introduce a gaussian diffusion coefficient $\delta(r)$ with a maximum at the center:

$$\delta(r) \equiv 1 + e^{-4r^2/9}. \tag{24}$$

The following substitution is made for incorporation into eqs. (19):

$$\nabla^2 \rightarrow \delta(r)\nabla^2. \tag{25}$$

The resulting system of equations is numerically solved in 2D with boundary conditions (15). The resulting stationary state at $t = 100$ is shown in Figure 9. The particle structure values are shown in Table 1 column 2Dδ. Note that in this case the core RMS radius for the φ_G potential increases by 38% and the full integral of φ_G potential becomes negative thus yielding a physically realistic positive gravitational mass.

It is possible that such core broadening might occur with the onset of a rotational wave mode similar to the spiral waves observed in the B-Z reaction. Mihalache (2011) describes simulations in which spiral waves form in the dissipative soliton produced by the complex, cubic-quintic Ginzburg-Landau system. With the emergence of the rotational wave state they find that the soliton's core broadens by 1.5 to 2 fold. We are currently unable to directly simulate Model G particles with rotational wave modes since, as mentioned earlier, limitations of our available computational resources required that we impose a symmetry condition when simulating in 2D and 3D.

4.3 *1D Particle Movement in a Gravitational Gradient*

The movement of a 1D particle is examined in the presence of a G-gradient. The G-gradient of slope m is incorporated into the system by adding the function

$$\gamma_m(x,t) = \begin{cases} 0 & \text{if } t < 100, \\ mx + 10^{-4}/6 & \text{if } 100 \leq t \end{cases} \tag{26}$$

to the right-hand side of eq. (13a). This function allows the particle to form from $t = 0$ to 100, then "turns on" a G-gradient of slope m from $t = 100$ to 200, during which time we examine the particle's positions and velocities.

Using the parameter substitutions again of eqs. (17) and solving the resulting system of PDEs under the boundary conditions

$$\forall x \in [-50, 50] : \forall t \in [0, 200] :$$

$$\alpha = 3875/4096 \tag{27a}$$

$$\varphi_G(x,0) = -0.161\alpha e^{-\frac{1}{2}\left(\frac{x}{0.363}\right)^2} \tag{27b}$$

$$\varphi_X(x,0) = -8.37\alpha e^{-\frac{1}{2}\left(\frac{x}{0.272}\right)^2} \tag{27c}$$

$$\varphi_Y(x,0) = 0.930\alpha e^{-\frac{1}{2}\left(\frac{x}{0.302}\right)^2} \tag{27d}$$

$$\varphi_G(\pm 50, t) = \gamma_m(\pm 50, t) \tag{27e}$$

$$\varphi_X(\pm 50, t) = 0 \tag{27f}$$

$$\varphi_Y(\pm 50, t) = 0 \tag{27g}$$

yields the same single-particle state of Figure 7(a) as done previously. The difference here is that the particle grows from gaussian initial conditions eqs. (27b, 27c, 27d)[1] rather than the seed fluctuation χ. The purpose of using these initial conditions is that eqs. (27) produce the particle more quickly than χ does. If we were instead to use the χ fluctuation, the 1D particle would still be "settling down" at $t = 100$ with its core zeroes still moving on the order of 10^{-6} per unit time. This is the approximate magnitude of the particle velocities due to the induced G-gradients. In contrast, the 1D particle created from these alternate initial conditions has its core zeroes effectively stationary at this order of magnitude, allowing us to measure the particle's velocity in isolation of this settling effect.

The 11 values for the G-gradients m that are examined are $m = -10^{-5}k/3$ for $k \in \{0, 1, 2, ..., 10\}$. See Figures 10. The position of the particle is defined to be the midpoint between the two center-most zeroes of φ_X flanking its central minimum. This was found to be a more precise method of determining the particle's position than simply calculating the location of the central minimum of φ_X, due to the fact that $\varphi_X(x,t)$ is a numerical solution to the PDEs in this present analysis, and any specific value is numerically interpolated. Thus points along highly sloping areas of φ_X, such as its zeroes, are more accurately interpolated than local extrema, whose precise locations must generally be extrapolated. The initial hills in Figure 10(b) are an artifact of this method of determining the particle's position, as the form of the particle is slightly altered by the applied G-gradient. Because of this, the

[1]Note the use of the *Core amplitude* and *Core RMS radius* values from Table 1 in these 3 equations. The constant α is an overall factor used to select initial conditions that create the particle in as little time t as possible.

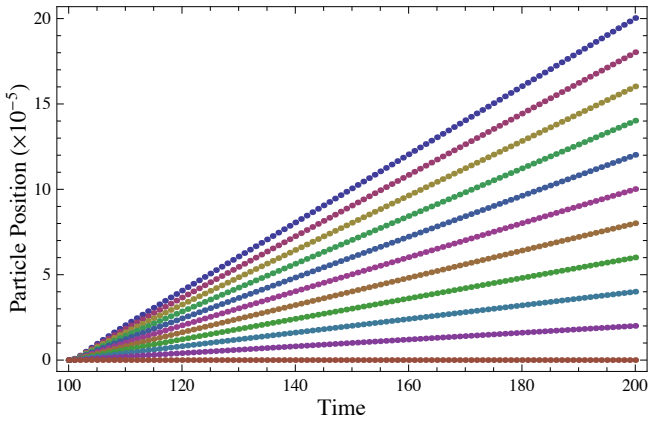

(a) 1D particle positions in 11 different G-gradients.

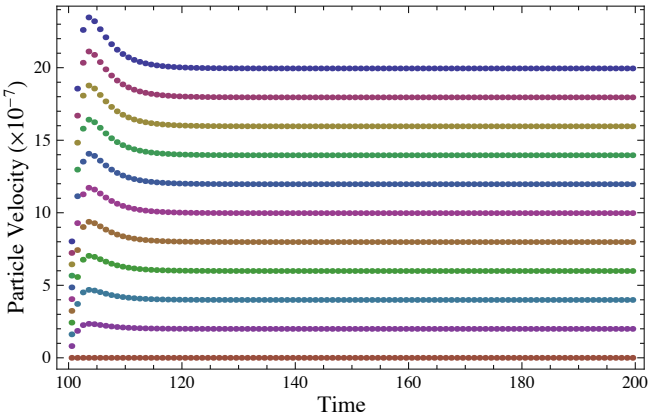

(b) 1D particle velocities in 11 different G-gradients.

Figure 10. Positions (a) and velocities (b) of the 1D particle from $t = 100$ to 200 for 11 different values of the G-gradient $m = -10^{-5}k/3$ for $k = 0, 1, 2, ..., 10$, corresponding to the data sets displayed from bottom–up, respectively. After the G-gradient is turned on at $t = 100$, the particle velocity converges to a constant value, proportional to the applied G-gradient m.

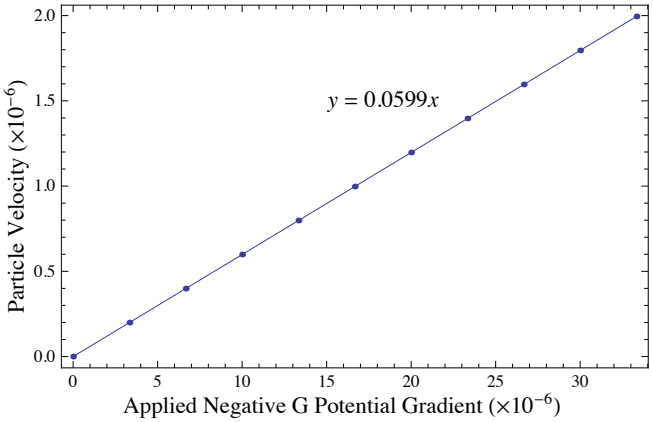

Figure 11. The 1D particle's constant velocities vs. the 11 values of the applied G-gradient m form a linear relationship.

average of the velocities from $t = 150$ to 200 are used in the particle velocity vs. G-gradient plot shown in Figure 11. The 11 velocities v were found to be directly proportional to the applied G-gradient m:

$$v = -0.0599m. \tag{28}$$

To realistically represent microphysical phenomena, Model G would need to spawn solitons that accelerate in a G-gradient field rather than move at a constant velocity. There are many aspects of Model G that still remain unexplored and we feel that future work will demonstrate particle acceleration. In particular, future 3D simulations of Model G will investigate whether 3D solitons incorporating rotational wave modes will be found to accelerate in G-gradients.

5. Conclusion

Features of Model G's solitons in one, two, and three dimensions of space were examined, and found to have characteristics resembling those observed for subatomic particles. These include a structure matching observations of the nucleon's stationary wave charge distribution, multi-particle bonding, and movement in field gradients. Model G was derived from the Brusselator R-D system using a recipe general enough to potentially generate new soliton-supporting systems from R-D systems that are unable to. All such systems would be interesting candidates to study in the context of the subquantum kinetics methodology.

Acknowledgments

MP would like to thank Kerry Cassidy and Bill Ryan of Project Camelot for their interview of Paul LaViolette in July of 2009.

Appendix A. Brusselator Solitons

Here we describe one other way of modifying the Brusselator in order for it to support dissipative solitons. This involves keeping the reaction system with just four reactions, as it was originally specified, but allowing A to vary in addition to X and Y, and allowing non-zero reverse reaction rates for A $\leftarrow$ X and X $\leftarrow$ E. We begin with the reversible Brusselator, which is specified by the following kinetic reactions (Nicolis and Prigogine, 1977):

$$\mathrm{A} \underset{k_{-1}}{\overset{k_1}{\rightleftharpoons}} \mathrm{X} \tag{A1a}$$

$$\mathrm{B} + \mathrm{X} \underset{k_{-2}}{\overset{k_2}{\rightleftharpoons}} \mathrm{Y} + \mathrm{D} \tag{A1b}$$

$$2\mathrm{X} + \mathrm{Y} \underset{k_{-3}}{\overset{k_3}{\rightleftharpoons}} 3\mathrm{X} \tag{A1c}$$

$$\mathrm{X} \underset{k_{-4}}{\overset{k_4}{\rightleftharpoons}} \mathrm{E}. \tag{A1d}$$

Expressed as PDEs with diffusion:

$$\frac{\partial \mathrm{A}}{\partial \mathrm{t}} = D_{\mathrm{A}}\nabla^2\mathrm{A} - k_1\mathrm{A} + k_{-1}\mathrm{X} \tag{A2a}$$

$$\begin{aligned}\frac{\partial \mathrm{X}}{\partial \mathrm{t}} &= D_{\mathrm{X}}\nabla^2\mathrm{X} + k_1\mathrm{A} + k_{-4}\mathrm{E} + k_{-2}\mathrm{DY} \\ &\quad - (k_{-1} + k_2\mathrm{B} + k_4)\mathrm{X} + k_3\mathrm{X}^2\mathrm{Y} - k_{-3}\mathrm{X}^3\end{aligned} \tag{A2b}$$

$$\frac{\partial \mathrm{Y}}{\partial \mathrm{t}} = D_{\mathrm{Y}}\nabla^2\mathrm{Y} - k_{-2}\mathrm{DY} + k_2\mathrm{BX} - k_3\mathrm{X}^2\mathrm{Y} + k_{-3}\mathrm{X}^3. \tag{A2c}$$

Passing to a dimensionless system, the units of time, space, and concentration are identified, respectively, as:

$$\mathrm{T} \equiv \frac{1}{k_{-1}+k_4}, \quad \mathrm{L} \equiv \sqrt{D_{\mathrm{A}}\mathrm{T}}, \quad \mathrm{C} \equiv \frac{1}{\sqrt{k_3\mathrm{T}}}. \tag{A3}$$

These are used to replace the dimensional parameters with their dimensionless counterparts, as done in eqs. (5). Together with the dimensionless parameter substitutions

$$\begin{aligned} d_{\mathrm{x}} &\equiv \frac{D_{\mathrm{X}}}{D_{\mathrm{A}}}, \quad d_{\mathrm{y}} \equiv \frac{D_{\mathrm{Y}}}{D_{\mathrm{A}}}, \quad b \equiv \frac{k_2}{k_{-1}+k_4}\mathrm{B}, \quad g \equiv \frac{k_{-1}}{k_{-1}+k_4}, \\ p &\equiv \frac{k_1}{k_{-1}+k_4}, \quad s \equiv \frac{k_{-3}}{k_3}, \quad u \equiv \frac{k_{-2}}{k_{-1}+k_4}\mathrm{D}, \quad w \equiv \frac{\sqrt{k_3}k_{-4}}{(k_{-1}+k_4)^{3/2}}\mathrm{E}\end{aligned} \tag{A4}$$

eqs. (A2) become

$$\frac{\partial A}{\partial t} = \nabla^2 A - pA + gX \tag{A5a}$$

$$\frac{\partial X}{\partial t} = d_{\mathrm{x}}\nabla^2 X + pA + w + uY - (1+b)X + X^2Y - sX^3 \tag{A5b}$$

$$\frac{\partial Y}{\partial t} = d_{\mathrm{y}}\nabla^2 Y - uY + bX - X^2Y + sX^3. \tag{A5c}$$

We again use the same vector operator ∇ in both equation sets (A2,A5) with the understanding that the prior is taken with respect to dimensional units, and the latter dimensionless.

The homogeneous steady state values for A, X, and Y are, respectively,

$$A_0 = \frac{gw}{p(1-g)}, \quad X_0 = \frac{w}{1-g}, \quad Y_0 = \frac{sX_0^2 + b}{X_0^2 + u}X_0. \tag{A6}$$

Defining the concentration potentials

$$\varphi_A \equiv A - A_0, \quad \varphi_X \equiv X - X_0, \quad \varphi_Y \equiv Y - Y_0 \tag{A7}$$

and additional system constants

$$\begin{aligned} c_0 &\equiv X_0^2 + u, & c_1 &\equiv b - 2X_0Y_0 + 3sX_0^2, \\ c_2 &\equiv 2X_0, & c_3 &\equiv Y_0 - 3sX_0 \end{aligned} \tag{A8}$$

yields

$$\frac{\partial \varphi_A}{\partial t} = \nabla^2 \varphi_A - p\varphi_A + g\varphi_X \tag{A9a}$$

$$\frac{\partial \varphi_X}{\partial t} = d_{\mathrm{x}} \nabla^2 \varphi_X + p\varphi_A - \varphi_X + c_0 \varphi_Y + (c_2 \varphi_Y - c_1 + (\varphi_Y + c_3 - s\varphi_X)\varphi_X)\varphi_X \tag{A9b}$$

$$\frac{\partial \varphi_Y}{\partial t} = d_{\mathrm{y}} \nabla^2 \varphi_Y - c_0 \varphi_Y - (c_2 \varphi_Y - c_1 + (\varphi_Y + c_3 - s\varphi_X)\varphi_X)\varphi_X. \tag{A9c}$$

Solving this system in 1D with boundary conditions

$$\begin{aligned} &\forall x \in [-50, 50] : \forall t \in [0, 100] : \\ &\qquad \varphi_A(x,0) = -0.161 e^{-\frac{1}{2}\left(\frac{x}{0.363}\right)^2} \\ &\qquad \varphi_X(x,0) = -8.37 e^{-\frac{1}{2}\left(\frac{x}{0.272}\right)^2} \\ &\qquad \varphi_Y(x,0) = 0.930 e^{-\frac{1}{2}\left(\frac{x}{0.302}\right)^2} \\ &\varphi_A(\pm 50, t) = 0 \\ &\varphi_X(\pm 50, t) = 0 \\ &\varphi_Y(\pm 50, t) = 0 \end{aligned} \tag{A10}$$

and dimensionless parameter values

$$\begin{aligned} d_{\mathrm{x}} = 1, \quad d_{\mathrm{y}} = 12, \quad b = 29, \quad g = 1/10, \\ p = 1, \quad s = 0, \quad u = 0, \quad w = 14 \end{aligned} \tag{A11}$$

at $t = 100$ yields the same soliton configuration shown in Figure 7(a), with φ_G replaced by φ_A. Throughout the reaction, all concentrations maintain a non-negative value, equivalent to the conditions $\varphi_A \geq -A_0$, $\varphi_X \geq -X_0$, and $\varphi_Y \geq -Y_0$.

The same 2D and 3D soliton configurations are found as with Model G, when circular and spherical symmetry are imposed, and with the following modifications:

- The 3 gaussian initial conditions in eqs. (A10) have their heights and widths, which are the values from rows (a) and (c) from Table 1, modified using the corresponding 2D or 3D column.
- The Dirichlet boundary conditions at $x = -50$ for 1D are replaced by the Neumann boundary conditions at $r = 0$ for 2D and 3D, as done in equation sets (14,15).

References

Bode, M., Liehr, A., Schenk, C. and Purwins, H.G., 2002. Interaction of dissipative solitons: particle-like behaviour of localized structures in a three-component reaction-diffusion system. *Physica D: Nonlinear Phenomena*, 161 (1–2), 45–66.

Bödeker, H.U., 2007. Universal Properties of Self-Organized Localized Structures. Thesis (PhD). Universität Münster.

Herschkowitz-Kaufman, M. and Nicolis, G., 1972. Localized Spatial Structures and Nonlinear Chemical Waves in Dissipative Systems. *J. of Chemical Physics*, 56 (5), 1890–1896.

Kelly, J.J., 2002. Nucleon Charge and Magnetization Densities from Sachs Form Factors. *Physical Review C*, 66 (6), 065203.

Koga, S. and Kuramoto, Y., 1980. Localized Patterns in Reaction-Diffusion Systems. *Progress of Theoretical Physics*, 63 (1), 106–121.

LaViolette, P.A., 1985. An Introduction To Subquantum Kinetics: Parts I, II, III. *Intern. J. of General Systems*, 11 (4), 281–345.

LaViolette, P.A., 1986. Is The Universe Really Expanding? *Astrophysical J.*, 301, 544–553.

LaViolette, P.A., 1992. The Planetary-Stellar Mass-Luminosity Relation: Possible Evidence of Energy Nonconservation? *Physics Essays*, 5 (4), 536–544.

LaViolette, P.A., 1994. *Subquantum Kinetics: The Alchemy of Creation*. 1st ed. Alexandria, VA: Starlane Publications (out of print).

LaViolette, P.A., 2005. The Pioneer Maser Signal Anomaly: Possible Confirmation of Spontaneous Photon Blueshifting. *Physics Essays*, 18 (2), 150–163.

LaViolette, P.A., 2008. The Electric Charge and Magnetisation Distribution of The Nucleon: Evidence of A Subatomic Turing Wave Pattern. *Intern. J. of General Systems*, 37 (6), 649–676.

LaViolette, P.A., 2010. *Subquantum Kinetics: A Systems Approach to Physics and Astronomy*. 3rd ed. Niskayuna, NY: Starlane Publications.

LaViolette, P.A., 2012. *Subquantum Kinetics: A Systems Approach to Physics and Astronomy*. 4th ebook ed. Niskayuna, NY: Starlane Publications.

Lefever, R., 1968. Dissipative Structures in Chemical Systems. *J. of Chemical Physics*, 49 (11), 4977–4978.

Liehr, A.W., *et al.*, 2003. Replication of Dissipative Solitons by Many-Particle Interaction. *In*: *High Performance Computing in Science and Engineering '02.*, 48–61 Berlin: Springer.

Liehr, A., *et al.*, 2004. Rotating bound states of dissipative solitons in systems of reaction-diffusion type. *The European Physical J. B: Condensed Matter and Complex Systems*, 37, 199–204.

Mihalache, D., 2011. Spiral solitons in two-dimensional complex cubic-quintic Ginzburg-Landau models. *Romanian Reports in Physics*, 63 (2), 325–338.

Nicolis, G. and Prigogine, I., 1977. *Self-Organization in Nonequilibrium Systems: From Dissipative Structures to Order Through Fluctuations*. New York: John Wiley & Sons.

Nishiura, Y., Teramoto, T. and Ueda, K.I., 2005. Scattering of traveling spots in dissipative systems. *Chaos*, 15 (4), 047509.

Purwins, H.G., Bödeker, H. and Liehr, A., 2005. Dissipative Solitons in Reaction-Diffusion Systems. *Lecture Notes in Physics*, 661, 267–308.

Schenk, C.P., Schütz, P., Bode, M. and Purwins, H.G., 1998. Interaction of self-organized quasiparticles in a two-dimensional reaction-diffusion system: The formation of molecules. *Physical Review E*, 57, 6480–6486.

Turing, A.M., 1952. The Chemical Basis of Morphogenesis. *Philosophical Trans. of the Royal Society of London B: Biological Sciences*, 237 (641), 37–72.

Vanag, V.K. and Epstein, I.R., 2007. Localized Patterns in Reaction-Diffusion Systems. *Chaos*, 17 (3), 037110.

Winfree, A.T., 1974. Rotating Chemical Reactions. *Scientific American*, 230, 82–95.

Zaikin, A.N. and Zhabotinsky, A.M., 1970. Concentration Wave Propagation in Two-dimensional Liquid-phase Self-oscillating System. *Nature*, 225, 535–537.